World Electric Vehicle Journal

MDPI

Article

Evaluation of Vehicle Lateral and Longitudinal Dynamic Behavior of the New Package-Saving Multi-Link Torsion Axle (MLTA) for BEVs

Jens Olschewski * and Xiangfan Fang

Institute of Automotive Lightweight Design, University of Siegen, Breite Str. 11, 57076 Siegen, Germany; xiangfan.fang@uni-siegen.de

* Correspondence: jens.olschewski@uni-siegen.de

Abstract: To increase the package space for the battery pack in the rear of battery electric vehicles (BEVs), and thus extend their driving range, a novel rear axle concept called the multi-link torsion axle (MLTA) has been developed. In this work, the kinematic design was extended with an elastokinematic concept, and the MLTA was designed in CAD and realized as a prototype. It was then integrated into a B-class series-production vehicle by adding masses in different locations of the vehicle to replicate the mass distribution of a BEV. Both objective and subjective vehicle dynamic evaluations were conducted, which included kinematic and compliance tests, constant-radius cornering, straight-line braking, and a frequency response test, as well as subjective evaluations by both expert and normal drivers. These test results were analyzed and compared to a production vehicle. It can be concluded that the vehicle dynamic performance of the MLTA-equipped vehicle is, overall, 0.67 grades lower than that of the comparable production vehicle on a 10-grade scale. According to OEM experts, this deficit can be eliminated by tuning the different components of the MLTA and meeting the tolerance requirements of series production vehicles.

Keywords: new rear axle concept; suspension systems; electric vehicles; BEVs; objective driving test; subjective evaluation

check for updates

Citation: Olschewski, J.; Fang, X. Evaluation of Vehicle Lateral and Longitudinal Dynamic Behavior of the New Package-Saving Multi-Link Torsion Axle (MLTA) for BEVs. *World Electr. Veh. J.* **2024**, *15*, 310. https://doi.org/10.3390/wevj15070310

Academic Editor: Ayman EL-Refaie

Received: 24 May 2024
Revised: 5 July 2024
Accepted: 9 July 2024
Published: 15 July 2024

Copyright: © 2024 by the authors. Licensee MDPI, Basel, Switzerland. This article is an open access article distributed under the terms and conditions of the Creative Commons Attribution (CC BY) license (https://creativecommons.org/licenses/by/4.0/).

1. Introduction

1.1. State of the Art

To meet the increasing challenges brought about through climate change, the EU introduced a legislative package in 2021 called Fit for [1]. As a result, only CO_2-neutral cars will be allowed to be registered starting from 2035. To achieve this goal, there must be a strong market penetration of CO_2-neutral drive technologies in all vehicle segments. In recent years, battery electric vehicles (BEVs) have proven to be the key technology in this area. A crucial factor for market acceptance and, therefore, buying behavior is the range of BEVs. This is particularly evident in the A–C vehicle segment, where package space restrictions have led to small battery sizes. The German registration numbers from 2021 have shown that the TBA has the greatest spread in the A–C vehicle segment for BEVs [2].

For this kind of vehicle, the torsion beam of TBA limits the available package space toward the rear, as can be seen in Figure 1.

The package space behind the torsion beam (indicated in orange) for the battery pack is normally unused due to safety issues. It is obvious that the TBA shows only limited design potential to create more space for the battery. Wilmes et al. [3] have presented a BEV concept with a torsion crank axle with a torsion beam almost in the middle of the wheel center that is supported in a lateral direction with Watt's linkage (Figure 2a). In this way, the package space for the drive battery can be extended in the range of 10–15%.

In 2015, ZF presented the composite leaf spring axle (CLA), which uses a laterally oriented leaf spring made out of glass fiber-reinforced plastic (GFRP) [4] (Figure 2b). The

CLA is based on the McPherson principle, while the conventional lower control arm is replaced with the laterally oriented leaf spring (green) and a longitudinal control arm. In addition, a toe link and a wheel-guided damper are used to guide the wheel. With this design, up to 70 mm in the longitudinal direction can be gained in the rear area of the car. This concept was further developed by Ditzer et al. [5], shown in Figure 2c. In their design, only a wheel-guided damper combined with a GFRP leaf spring (green) was needed to guide the wheel. The elastokinematic could be modified because of the GFRP design, which achieved similar lateral and longitudinal compliance compared with a multi-link axle while reducing the number of components and the axle weight [5].

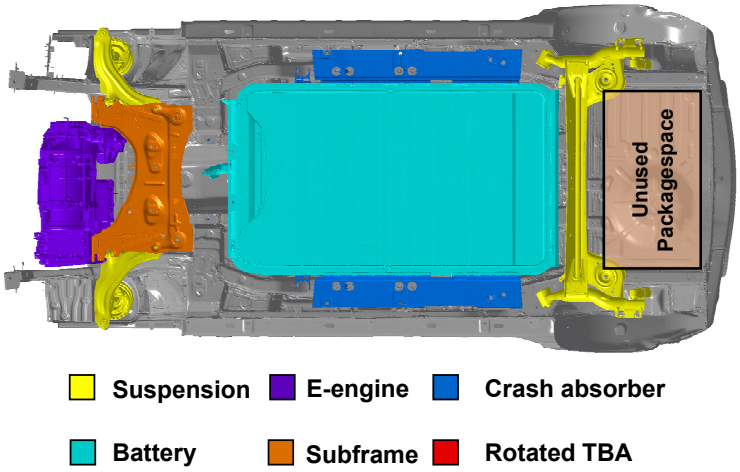


Figure 1. Underbody of the Renault Zoe with TBA rear suspension; unused package space indicated with an orange box.

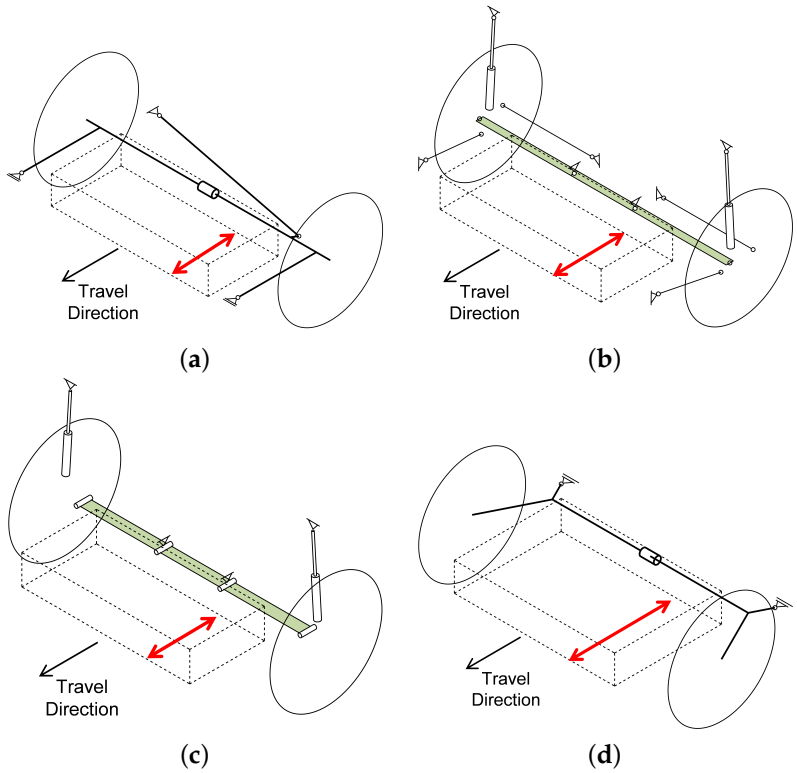


Figure 2. Package space-saving rear axles; increase in package space compared to conventional TBA is indicated by red arrows: (**a**) torsion-crank axle with Watt's linkage; (**b**) composite leaf spring axle of ZF [4]; (**c**) composite leaf spring axle by Ditzer et al. [5]; (**d**) reversed twist beam axle to increase package space behind the wheel center [6].

1.2. The Concept of the Novel Multi-Link Torsion Axle

As shown in Section 1.1, the torsion crank axle may extend the battery package space up to the wc, but the space behind the wheel center (WC) is still unused. Therefore, Fang proposed to reverse the installation of the TBA, as shown in Figure 2d [6]. This modification provides a significant expansion of the package space behind the WC, enabling larger battery packs, thereby increasing the range for battery electric vehicles (BEVs). However, this reversal of the TBA has the disadvantage of a highly increased pitch angle θ during braking, which is not accepted by the customer.

This behavior can be seen in Figure 3a, which shows the reaction forces on the reversed TBA during a braking maneuver. The braking force, F_x, acts at the wheel patch (WP), while the dynamic load transfer causes a change in wheel load, ΔF_z. The resulting force vector, $\underline{F}_{res}$, is the sum of these forces. To achieve a static equilibrium state, the suspension, $\underline{F}_{susp}$, and the spring force, $\underline{F}_{SP,WCA}$, at the wheel carrier (WCA) must counteract the resulting force, $\underline{F}_{res}$. The spring force can be calculated with the unit vector in spring direction $\underline{e}_{SP}$, the brake support angle, ε_{Br}, which results from the geometry, and the ideal break support angle, ε_i, resulting from the forces and the kinematic ratio, i_{SP}, between the WC and spring. It can be calculated with the following equation:

$$\underline{F}_{SP,WCA} = i_{SP} \cdot \underline{e}_{SP} \cdot F_x \cdot [tan(\varepsilon_i) - tan(\varepsilon_{Br})] = i_{SP} \cdot \underline{e}_{SP} \cdot F_{z,SP,WP} \tag{1}$$

It clearly can be seen that the position of the instantaneous center of motion (IC) behind the WC results in a positive angle of brake support, denoted as ε_{Br}:

$$\varepsilon_{Br} = -atan(\Delta_{IC_z} / \Delta_{IC_x}) \tag{2}$$

The IC position results in the vertical force component $F_{z,susp}$ in the same direction as the wheel load transfer, ΔF_z, as shown in Figure 3a. As a result, this suspension geometry amplifies the force $F_{z,SP,WP}$, which must be counteracted via the spring force. So, this configuration leads to increased spring compression, resulting in a high pitching angle θ during braking.

The vertical force $F_{z,susp}$, which needs to be countered via the suspension, can be related to the overall resulting force, which results in a negative anti-lift ratio κ_r for the rear axle:

$$\kappa_r = \frac{-F_{z,susp}}{\Delta F_z} \cdot \% = \frac{tan(\varepsilon_i)}{tan(\varepsilon_{Br})} \cdot \% \tag{3}$$

To avoid this negative characteristic, Niessing, Fang, and Schlichting [7] proposed a new axle concept called MLTA. In this design, the reversed TBA (referred to as the twist beam equivalent (TBE)) is additionally guided via a longitudinally oriented Watt's linkage, as shown in Figure 3b.

The MLTA concept decouples the instantaneous center of motion (IC) of the wheel carrier (WCA) and the WC from the rear attachment position U. The IC is formed at the intersection of the two virtually extended control arms, so it can easily be positioned in front of the WC in the driving direction. According to Equations (2) and (3), this will result in a positive anti-lift ratio because of a changed sign of ε_{Br}. This can also be seen in Figure 3b, where a portion of the resulting force is counteracted via the suspension force $F_{z,susp}$.

Figure 3c shows the kinematic equivalent model of the MLTA in an isometric view. It consists of six parts: the left and right twist beam equivalent (TBE), connected via a revolute joint at the shear center (SC) with two additional in-plane degrees of freedom (DOFs) indicated with arrows. Each TBE side is connected to the body in white (BIW) with a spherical joint at the upper body mount (U), with an additional in-line DOF. The left and right WCA are connected to the TBE with a revolute joint at the upper wheel carrier point (RU), and they are also guided via the longitudinal link (LL) with spherical joints at the lower wheel carrier point (RL) and lower body mount (L). In sum, the model comprises six spherical joints, three revolute joints, one in-plane joint, and two in-line joints, resulting in two DOFs. The ω_{pwt} axis represents the DOF for parallel wheel travel (PWT), while the

ω_{owt} axis approximates the DOF for opposite wheel travel (OWT) during roll motion. In addition to the kinematic consideration, each wheel is connected to the WCA via a revolute joint at the WC position, representing the wheel spindle.

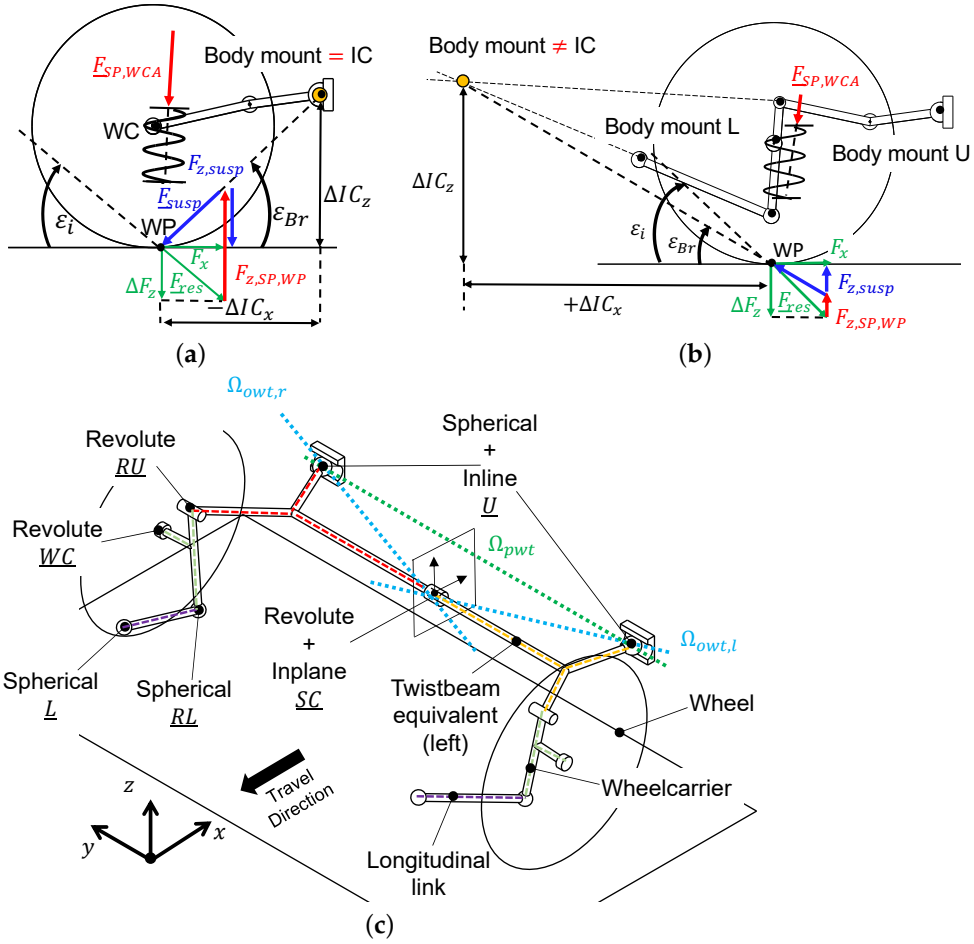


Figure 3. Reversed TBA and MLTA in comparison: (**a**) side view of a reversed TBA under braking force conditions; IC is equal to the body-mount position U. (**b**) Side view of the MLTA under braking force conditions. IC is not equal to the body-mount positions U and L. (**c**) Kinematic equivalent model of MLTA in 3-dim view, twist beam equivalent (TBE) parts in red (right) and orange (left), WCA (green), LL (purple), Ω_{pwt} rotation axis for parallel wheel travel, and Ω_{owt} rotation axes for opposite wheel travel.

In a previous work by Niessing and Fang [7], the kinematic principle of the MLTA mechanism was analyzed in detail. An algorithm for the MLTA kinematic similar to that shown in Figure 3c was developed and subsequently integrated into an optimization algorithm. The objective of the optimization was to obtain the targeted kinematic properties of a series production TBA as a reference while taking into account the constraints defined by the available package space in the vehicle. The optimization resulted in a hard point configuration that satisfies both the requirements for the kinematic requirements and package space.

1.3. Research Subject

The target of the present work is to extend the previously developed kinematic concept with elastokinematic aspects and implement the virtual design of the MLTA to a hardware prototype that can be integrated into a real vehicle: a 2020 Ford Fiesta. The driving performance of this prototype vehicle should be quantified through various objective kinematic and compliance (KnC) and driving tests. Another target of the work is to analyze

the results of these tests and provide detailed insights into the prototype vehicle's lateral performance such as cornering, and longitudinal dynamic behavior concerning anti-lift, while the assessment of the vehicle's comfort will be addressed in a future publication. Furthermore, the subjective ratings by both experienced and normal drivers should be conducted. All results will be evaluated in comparison with a series-production Ford Fiesta with mass modifications applied to reflect the battery weight. The potential of the new MLTA should, thus, be determined.

2. Design, Modeling, and Full-Vehicle Integration of the MLTA

In the current section, the details of the realization of the MLTA concept into a prototype for evaluation and demonstration purposes will be shown. The overarching objective was to fabricate an MLTA prototype with the capability of integration into the demonstration vehicle. To achieve this, a number of different requirements were placed on the axle prototype, as well as on the test vehicle.

2.1. Compliance Analysis and Bushing Design

The first kinematic analysis of the MLTA mechanism in [7] showed that the RU Bushing (see Figure 4) needs to satisfy high stiffness requirements to fulfill the elasto-kinematic targets, especially to achieve low camber compliance. This is why subsequent work [8] has concentrated on a detailed evaluation and optimization of the compliance properties of the MLTA, based on the hard points optimized in [7].

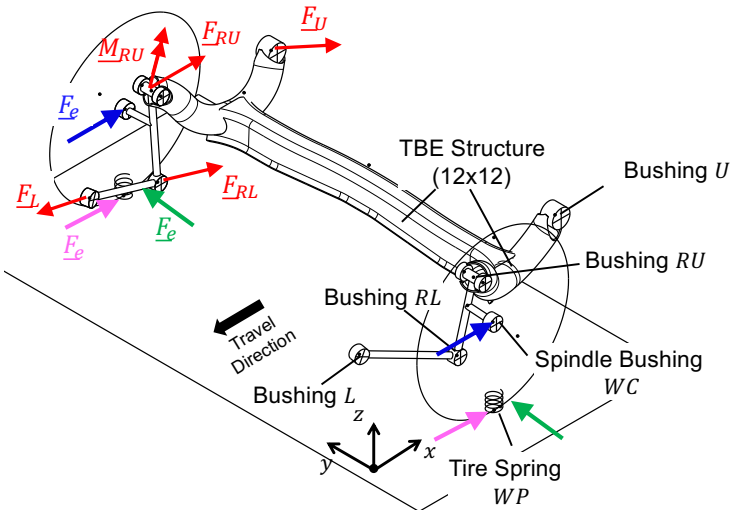


Figure 4. MLTA equipped with compliant bushings, with all kinematic joints from [7] replaced with bushings and rigid TBE bodies substituted with compliant TBE bodies, modeled using a 12 × 12 compliance matrix. The input force $\underline{F}_e$ is highlighted for the different load cases—green, LC1; blue, LC2; and magenta, LC3. The resulting reaction forces are shown in red.

Figure 4 shows the model used for the elastokinematic study. All kinematic joints in [7] were substituted with corresponding elastic bushings. In addition, the radial-tire compliance and the structural compliance of the wheel spindle were also integrated into the model via elastic bushings at their respective positions.

Additionally, the compliance of the TBE structure was determined through finite element method (FEM) analyses and integrated into the model using a 12 × 12 compliance matrix ($\mathbf{C}_{TBE}$). This thusly designed equivalent model replicates the boundary conditions of a kinematic and compliance (KnC) test rig.

Additionally, a modeling approach for the compliance analysis of suspension systems was developed. Details can be found in [8]. The joint reaction forces of the statically determined multibody system were formulated, and the solution was established using

MATLAB's symbolic Toolbox. This led to the coefficient matrix $\mathbf{A}_R$ and the constant vector $\underline{b}_R$, which enables the calculation of the global joint reaction force and moment vector $\underline{F}_R$:

$$\underline{F}_R = \mathbf{A}_R^{-1}\underline{b}_R \tag{4}$$

With these calculated joint reaction forces, principally shown in Figure 4, the deformation velocities at individual bushings could be determined. These velocities were then incorporated into the constant vector $\underline{b}_q$. Together with another coefficient matrix $\mathbf{A}_q$, the unknown velocities $\underline{\dot{q}}$ for the multibody system can be calculated. It was also formulated using MATLAB's symbolic Toolbox:

$$\underline{\dot{q}} = \mathbf{A}_q^{-1}\underline{b}_q \tag{5}$$

Subsequently, using the explicit Euler integration method, the deformations of the MLTA could be determined. More details can be found in [8].

In total, three different load cases, as shown in Figure 4, were evaluated with the optimized hard points shown in [7]:

- LC 1 (right cornering): $\underline{F}_e$ in y-direction at wheel patch (WP)
- LC 2 (obstacle crossing): $\underline{F}_e$ in x-direction at wheel center (WC)
- LC 3 (braking): $\underline{F}_e$ in x-direction at wheel patch (WP)

The calculation results of the joint reaction forces are shown in Table 1 (also see Figure 3c). It displays the reaction forces at each joint in relation to the input force $\underline{F}_e$ for the corresponding load cases, 1–3. It reveals that the RU bushing, in particular, must support very high cardanic moments due to the very high reaction forces in the z-direction, when lateral forces (LC1) are applied. Moreover, it clearly shows that the majority of the lateral force is transmitted to the body-in-white (BIW) through the rear bushing located at the U position. For load cases 2 and 3, it can be seen from Table 1 that the input forces in the x-direction are both considerably amplified in the longitudinal direction.

Table 1. Reaction forces relative to input force $\underline{F}_e$ (normalized as 100%) at design position.

	Right Cornering LC1			**Obstacle Crossing LC2**			**Braking LC 3**		
	X %	**Y %**	**Z %**	**X %**	**Y %**	**Z %**	**X %**	**Y %**	**Z %**
U	67	−200	37	−64	0	4	36	0	−2
RUi	−40	−50	−968	−281	0	−114	−392	−12	−388
RUo	40	−50	968	281	0	114	392	−12	388
WP	0	0	22	0	0	−19	0	0	−55
RL	1	0	0	−36	6	15	−136	24	57
L	1	0	0	−36	6	15	−136	24	57

This leads to the design constraints for the RU bushing that it should ensure both high cardanic and radial stiffness while minimizing the torsional rate to keep parasitic spring rates at a minimum. To meet these criteria, the RU bushing was divided into two individual bushings located at positions RUi and RUo, separated at a distance d_{RU}, as shown in Figure 5. In order to achieve the highest possible cardanic rate, the objective was to maximize the radial stiffness of both bushings while also maximizing the distance d_{RU} between them.

The maximum distance d_{PS} was particularly constrained due to the available package space, as shown in Figure 5. On the one side, this constraint was bounded due to the relative motion between the RU bushing and the side wall of the BIW. On the other side, the dimension of the RU bushing was restricted due to the brake disk.

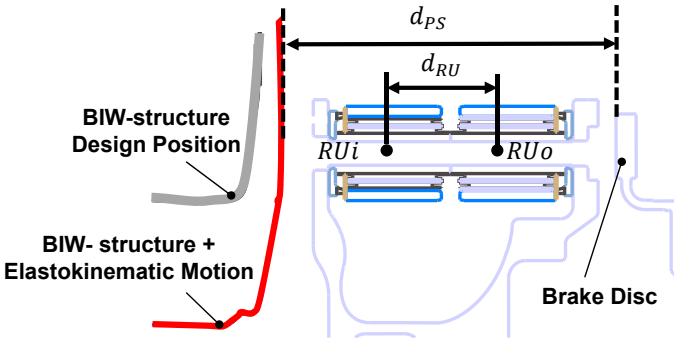


Figure 5. Package space for the integration of the RU bushing.

In addition, a Pareto optimization of the rear U bushing with respect to stiffness and spatial orientation was conducted using the calculation approach from Equations (4) and (5) [8]. It results in a new kind of bushing spatial orientation, as shown in Figure 6a. Instead of the usual practice of rotating the bushing around the global vehicle z-axis, the optimization proposes to rotate the bushing around the global vehicle x-axis as well. Through this x-rotation, a camber-compensating effect (the camber angle turns negative under lateral force) could be created, improving the camber stiffness of the MLTA. Additionally, other sources of compliance, such as the wheel spindle (WC) and the TBE structure, were identified. The radial tire stiffness also influences the measured overall compliance. Under the influence of the forces in the individual load cases (LC1–LC3), a reaction force acts in the vertical tire direction (Table 1), resulting in a change in the wheel position and orientation.

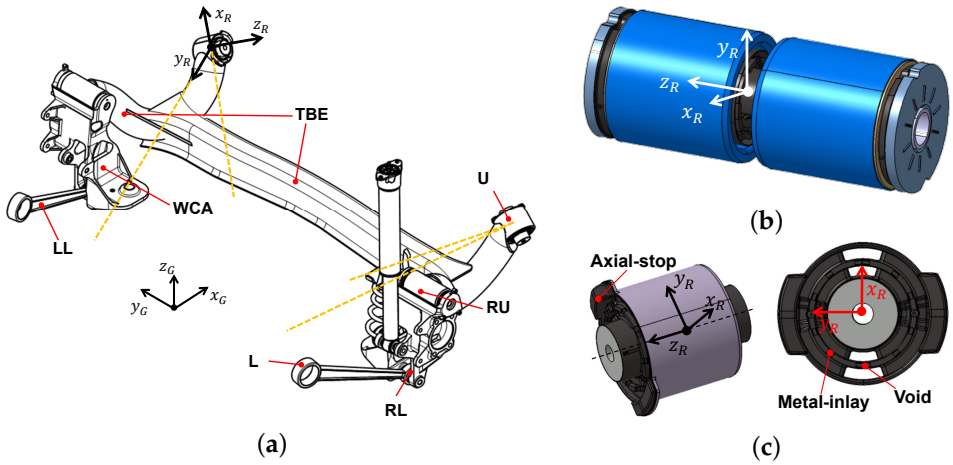


Figure 6. (**a**) Final designed CAD model of the MLTA; (**b**) upper wheel carrier point middle (RU) bushing—designed to obtain a high cardanic stiffness around the x_R and y_R axis; (**c**) upper body mount (U) bushing with axial stop and void in the more compliant direction, x_R

The individual influences of all relevant components of the MLTA can be calculated and optimized within the available package in the reference vehicle Ford Fiesta 2020 by changing the design and orientation of the components, as shown in Table 2. It can be seen that the RU bushing has a significant contribution to the lateral compliance, c_y, in load case 1. The same can be said about the U bushing. Furthermore, the RU bushing is crucial for the camber compliance in this load case. As a reference, the values of the conventional TBA are provided in Table 2 for comparison. It can be seen that the calculated and optimizable compliances of the MLTA are smaller than the values of the reference vehicle in two cases (LC1—$c\delta$; LC2—c_x) and slightly larger in three other cases (LC1—c_y, $c\gamma$; LC3—$c\theta$). According to consultations with OEMs, these values fall within the targeted range, classifying them as suitable for series production.

Table 2. Compliance contributions of each component of MLTA at three different load cases: $c\gamma$—camber compliance in deg/kN; $c\delta$—toe compliance in deg/kN; c_y—lateral compliance in mm/kN; c_x—longitudinal compliance in mm/kN; and $c\theta$—windup compliance in deg/kN.

	LC1 $c\gamma$	**LC1** $c\delta$	**LC1** c_y	**LC2** c_x	**LC3** $c\theta$
RU	0.15	-4.93×10^{-3}	1.20	0.10	-3.43×10^{-2}
WC	0.06	0.006	0.30	1.00×10^{-6}	-1.00×10^{-6}
TBE	0.04	0.025	0.44	0.11	-6.90×10^{-3}
WP	0.03	-4.75×10^{-3}	0.18	0.14	-0.16
L	4.60×10^{-5}	-2.70×10^{-5}	2.63×10^{-4}	0.50	-1.06
RL	1.00×10^{-6}	-1.00×10^{-6} <	7.00×10^{-6}	0.01	-2.92×10^{-2}
U	-0.04	-0.03	1.04	0.07	-1.26×10^{-2}
SUM	0.24	-8.15×10^{-3}	3.16	0.95	-1.31
TBA (reference)	0.18	-5.5×10^{-2}	3.03	1.49	-0.72

2.2. Suspension Design and Manufacturing

After the concept had been completed, detailed part design was conducted. Figure 6a shows the CAD data, consisting of five main components. Component 1 is the welding assembly, which includes the twist beam and the two trailing arms. This assembly is similar to a conventional twist-beam axle (TBA), so it is called twist-beam equivalent (TBE), as mentioned previously. This assembly connects to components 2 and 3, the left and right wheel carriers (WCAs). Components 4–5 are defined as the two longitudinal links (LLs), pointing in the driving direction and completing the longitudinally oriented Watt's linkage.

2.2.1. Prototype Bushings

Each component is interconnected to the other and to the body in white (BIW) via the different elastomer bushings. Table 3 summarizes the bushing properties. The designed characteristics result in the corresponding compliance contributions shown in Table 2. The U and RU bushings were optimized as described above and specifically designed and manufactured by the project partner Vorwerk Autotec. However, the prototypical manufacturing of the RU and U bushings results in deviations between the optimized (designed) stiffness values and the actual measured stiffness values, as shown in Table 3. The spatial orientation of each bushing is given with the Euler angles according to the $z - x' - z''$ convention.

Kinematically, the RU bushing acts as a revolute joint, as shown in Figure 3c. Its design was developed to have the highest possible cardanic stiffness with respect to the x_R and y_R axis (k_4, k_5) in combination with the lowest possible torsional rate, k_6, around the axial direction z_R (Figure 6b). In comparison, the prototype RU bushing shows a significant reduction in the radial rates k_1 and k_2, resulting in a decrease in the cardanic rate (k_4 and k_5). Additionally, there is a substantial increase in the torsional rate k_6, which is doubled compared to the designed value, leading to an increased parasitic spring rate and, thus, an increased wheel rate (see Section 3.1).

The U bushing has a metal inlay and a void in the compliant radial direction x_R (Figure 6c) to create two distinct radial rates. The comparison between the designed and prototype characteristics reveals that the prototype U bushing exhibits a significant deviation in stiffness k_3 (z_R-direction) of 63%. Furthermore, there is an increase in the torsional rate of 78%.

The lower body mount (L) and lower wheel carrier point (RL) bushings were used from a serial-production, multi-link suspension of the VW MQB platform, and they remained unchanged.

It has to be noted that the deviation of the designed and achieved (prototype) bushing stiffness was caused by the restricted possibilities in the prototype manufacturing of

bushings and the varying elastomer properties. Its impact on the elastokinematic behavior will be evaluated in the subsequent kinematics and compliance (KnC) analysis.

Table 3. Comparison of designed and prototype bushing characteristics for the MLTA prototype (designed values are normalized as 100%).

	$k1$ $\frac{N}{mm}$	$k2$ $\frac{N}{mm}$	$k3$ $\frac{N}{mm}$	$k4$ $\frac{Nm}{deg}$	$k5$ $\frac{Nm}{deg}$	$k6$ $\frac{Nm}{deg}$	**Eulerangles** deg
U (designed)	100%	100%	100%	-	-	100%	348.7, 122.8, 114.7
U (prototype)	121%	107%	163%	-	-	178%	348.7, 122.8, 114.7
RU (designed)	100%	100%	100%	100%	100%	100%	180, 90, 0
RU (prototype)	80%	80%	95%	80%	80%	201%	180, 90, 0
RL	2×10^4	2×10^4	660	-	-	-	180, 90, 0
L	310	1730	175	-	-	-	169.9, 90, 202.6
WP	-	-	250	-	-	-	0, 0, 0
WC	-	-	-	4818	4818	-	180, 90, 0

2.2.2. Component Design

The manufacturing of the individual components was mainly realized by the project partners CP Tech, Mubea, and Schmedthenke Werkzeugbau (SWB). The development of the TBE body was particularly challenging in terms of the structural design and manufacturing process. Specifically, the torsion beam had to achieve the highest possible bending stiffness to meet the required elasto-kinematic targets while also fulfilling a torsion angle of $\pm 10^\circ$ for the half-length with a defined torsional rate [9,10]. The design was carried out in several iteration loops using the FEM. Afterwards, the torsion profile was manufactured in a deep drawing process using a prototype tool, which was designed and built by SWB. Finally, the torsion beam was manually welded with the two curved-shaped trailing arms at CP Tech. The wheel carrier was milled using an aluminum block for easier manufacturing. The longitudinal link was a sand-casting aluminum component.

Since all components were manually made as prototypes, the ability to control the tolerances of the total assembly was limited, and only a few pieces of the prototypes could be made. For example, the manually welded trailing arm was outside the allowable tolerances range of series production TBA. Along with the deviations in bushing stiffness mentioned in the last section, the tolerances of the MLTA influenced the results of both objective and subjective tests, as discussed later in Sections 3 and 4.

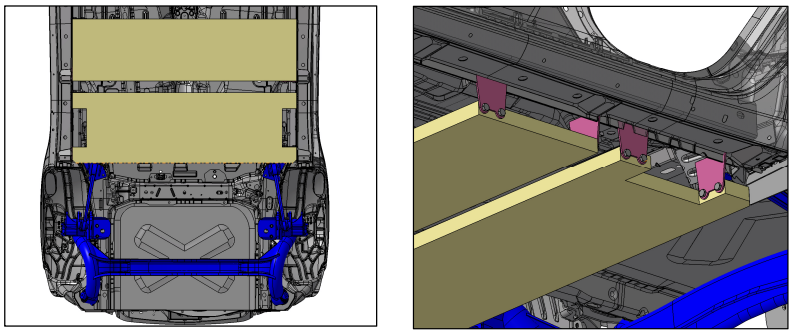
2.3. Full Vehicle—Design of the Battery Equivalent and Mass Properties

2.3.1. Vehicle Variants

The demonstration vehicle was a Ford Fiesta 2020 (8th Generation B479, 2017–2023) with an internal combustion engine (ICE). Three different vehicle setups were defined. The first setup, referred to as Variant A (Var_A), represents the production vehicle with standard rear suspension and no modifications. The multi-link torsion axle (MLTA) is intended to expand the space for batteries, as described above. Because the prototype vehicle has a combustion engine, the mass properties of a hypothetical BEV were represented using additional mass dummies as battery equivalents. That is why the second variant, referred to as Variant B (Var_B), takes into account the mass influences of a hypothetical battery pack with two mass dummies mounted onto the underbody (Figure 7a) and one mass dummy mounted in the trunk. They were mounted into the BIW with nearly no influence on the body stiffness (see Figure 7a). In this mass dummy design, the other aggregates of an ICE and BEV were also taken into account: the ICE aggregates (combustion engine and fuel tank) were removed and virtually substituted with BEV aggregates (an electric motor, a battery, and its management systems).

The third variant, referred to as Variant C (Var_C), was finally equipped with the MLTA. The mass properties between Var_B and Var_C remained unchanged, allowing a comparison of driving dynamics through a subjective evaluation described in Section 4. In this way, the

MLTA's influence on the lateral driving behavior can be investigated uncoupled from the mass influence.



(**a**) (**b**)

Figure 7. Prototype vehicle equipped with the MLTA (Var_C): (**a**) a mass dummy to represent the mass properties of a BEV based on the reference vehicle; (**b**) a detailed view of the 90-degree-rotated mass dummy attachment.

For the first design of the battery, a battery pack with eight modules that had a net energy content of 27.2 kWh was virtually placed into the body in white (BIW) CAD model of the Ford Fiesta (Figure 8a) [11]. To position the battery in the horizontal plane (xy), the surrounding vehicle structures were considered. As a result, the battery was positioned between the torsion profile of the originally equipped TBA (yellow) and the front (orange) subframes (Figure 8a). For realistic battery positioning in the vehicle's vertical direction, z_G, the position was mainly defined according to the limiting surface required for ground clearance.

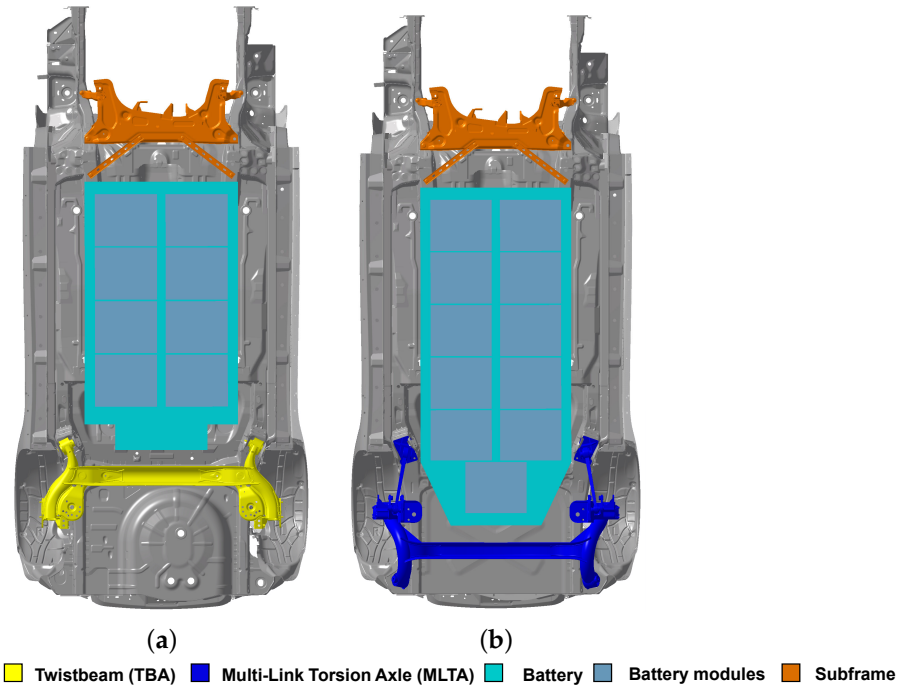


Figure 8. Underbody of the full vehicle: (**a**) view of the prototype vehicle underbody and conventional TBA equipped with the BMW i3 battery and 8 battery modules and (**b**) underbody with MLTA and 11 battery modules and a +30% total volume increase for battery cells.

In the same way, the battery package plan was conducted for MLTA, and Figure 8b shows that three modules may be added, which leads to an increase in the energy content of about 10.2 kWh. The utilization of the battery volume (volumetric energy density, Wh/L)

has increased rapidly in recent years [12,13]. The cell-to-pack design [14] and cell-to-body design [15] may especially enable a higher energy density.

Therefore, the total volume of the battery pack was considered as well, rather than the module size. The results indicate that the battery volume (as shown in Figure 8b) can be increased by 30%. When a power consumption of 15 kWh/100 km and a state-of-the-art volumetric energy density of 266 Wh/L [16] are assumed, this expansion could result in a range increase of about 115 km.

2.3.2. Mass Dummy Development

To analyze the influence of the battery pack mass m_{BP} on vehicle dynamics, mass dummies had to be developed and attached to the ICE vehicle. Because the vehicle is powered via an ICE, the mass of the combustion engine m_{ICE} and fuel tank m_{FT}, as well as the mass of a hypothetical electric engine, m_{EE}, and battery pack, m_{BP}, had to be considered in the design of the mass dummies. The overall weight, m_{MD}, of all mass dummies can be calculated using the following formula:

$$m_{MD} = m_{BP} + m_{EE} - m_{ICE} - m_{FT} \quad (6)$$

This results in a total mass of 320 kg for the mass dummy. In addition, the position of the new center of gravity, cg, was calculated and considered. The results of the different vehicle setups are shown in Table 4.

Table 4. Summary of the mass properties of the different vehicle variants in the 2UP load condition: Var_A original Ford Fiesta Vehicle, Var_B vehicle with installed mass dummies and standard TBA and Var_C vehicle with installed mass dummies and MLTA.

Vehicle Variant	Var_A	Var_B	Var_C
m_V Vehicle weight (kg)	1312	1643	1644
m_f Axle load front (kg)	781	876	872
m_r Axle load rear (kg)	531	767	772
Weight distribution	60%/40%	53%/47%	53%/47%
cg_x Center of gravity (rel.)	100%	106%	106%
cg_z Center of gravity (rel).	100%	86%	86%
I_{xx} (curb) (rel.)	100%	107%	107%
I_{yy} (curb) (rel.)	100%	117%	119%
I_{zz} (curb) (rel.)	100%	115%	119%

The integration of the MLTA prototype into the BIW was realized using a tubular frame (see Figure 9a) and corresponding attachment brackets for U and L. In addition, the spring and damper positions had to be adjusted for Var_C (see Figure 9b) because of package space restrictions. The design and hardware manufacturing was conducted by the project partner CP Tech.

To consider the changed mass properties, the front and rear suspension of Var_B and Var_C was equipped with a new spring and damper setup that was designed by Ford. The springs were adapted to the new axle loads (Table 4): the spring rate was increased by about 50% at the rear and 13% at the front to achieve approximately the same ride frequency of about 1.4 Hz as Var_A.

Due to the increased masses, the dampers also had to be adjusted. Additionally, the change in the damper hard points for Var_C changed the damper ratio (Figure 9b). Considering these effects, the dampers for Var_B and Var_C were adjusted so that they approximately achieve the same damping measure for the compression stage, D_{comp}, and rebound stage, $D_{rebound}$, as Var_A. Further details of the spring/damper design cannot be disclosed due to confidentiality reasons.



(**a**) (**b**)

Figure 9. Prototype vehicle equipped with the MLTA (Var_C): (**a**) tubular frame for the attachment of the MLTA; (**b**) Ford Fiesta modified with the MLTA prototype in a side view.

3. Objective Evaluation of the MLTA

3.1. Testing the Component-Level Kinematics and Compliance

The first step for the vehicle evaluation was the KnC test. During the KnC test, forces were applied at the wheel contact points via wheel-independent platforms that can be moved in the ground plane direction. The relative motion between the suspension and vehicle body is applied via a platform underneath the vehicle, which is connected to the BIW at four points on the rocker panel. Throughout the tests, wheel-individual forces and positions are measured by measuring arms and load cells (Figure 10). The ride height of the vehicle is adjusted according to the loading condition 2UP (driver + front passenger, without design luggage).

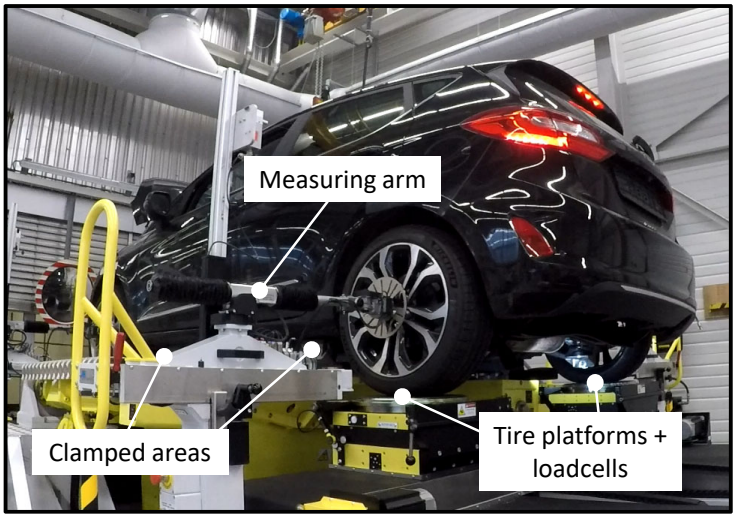


Figure 10. Vehicle with MLTA suspension on kinematic and compliance (KnC) test rig. The BIW is fixed to the test rig at the areas highlighted. Each tire stands on an individual moving platform. The wheel position and orientation are detected via the measuring arm.

Figure 11a shows the measured wheel rate c_{WC} during parallel wheel travel as a function of the relative wheel-center displacement for Variants B (black) and C (red).

To quantify the influence of deviation in bushing properties, the wheel rate was calculated approximately based on the kinematic results from [7] (also see the end of Section 1.2), as well as the spring stiffness (k_{SP}) and bushing torsional rates (k_6) from Table 3. Since the method in [7] was developed for kinematic calculations of the MLTA, only the values around the design position could be calculated with a good approximation. In the first step, the kinematic ratio for each bushing and spring element was calculated relative to the WC. For the bushing ratios, the velocity component in the local k_6-direction, as defined according to the Euler angles in Table 3, was considered. Similarly, for the spring ratio, the component of velocity in the direction of the spring was taken into account. Additionally, to incorporate the effect of spring preload forces, the preload (F_{SP}) was multiplied by the

spring's kinematic ratio gradient, as outlined in [17]. The overall wheel rate, c_{WC}, was then derived by summing the influences from all bushings (n) and the spring:

$$c_{WC} = \sum_{m=1}^{n} (k_{6,m} \cdot i_{Bush,m}^2) + k_{SP} \cdot i_{SP}^2 + F_{SP} \cdot \frac{di_{SP}}{dt} \quad (7)$$

The magenta line indicates the approximated wheel rate using the optimized (designed) bushing characteristics, while the light blue line shows the resulting wheel rate for the prototype bushing characteristics, as shown in Table 3.

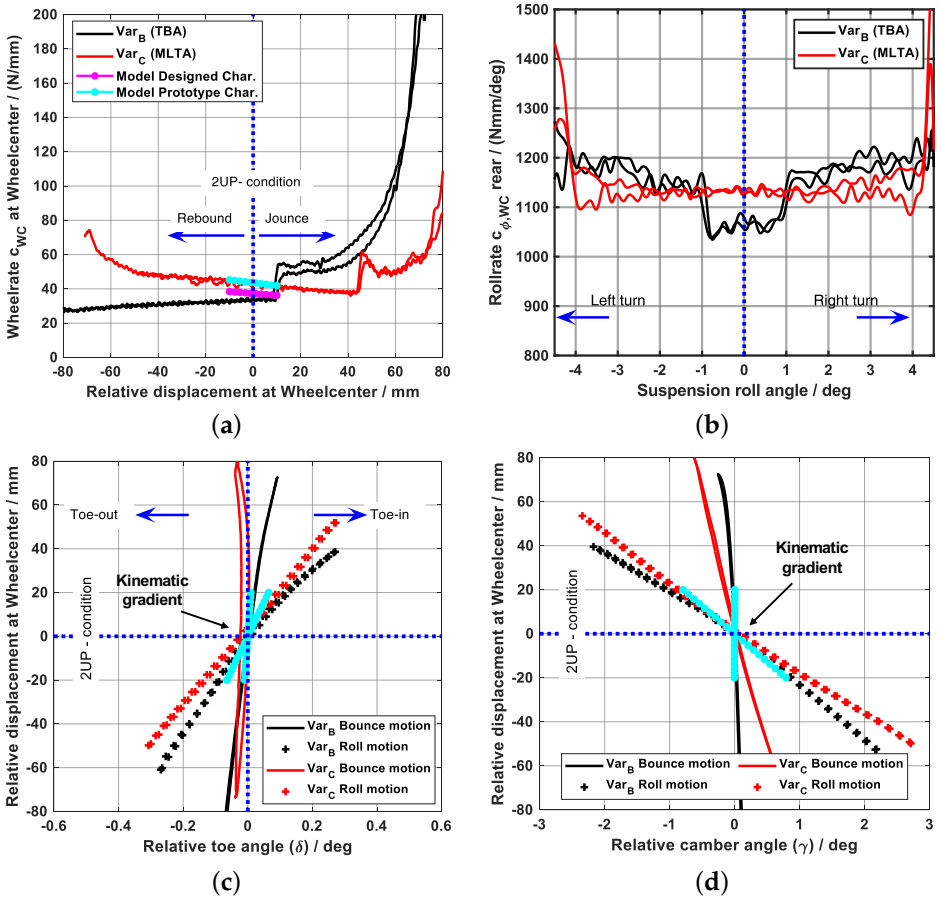


Figure 11. KnC results, comparison between Var_B and Var_C: (**a**) wheel rate during bounce motion and approximated wheel rate with designed bushing characteristics (magenta) and with prototype bushing characteristics (light blue), (**b**) roll rate during roll motion, (**c**) toe kinematic, and (**d**) camber kinematic for parallel and opposite wheel travel and gradients calculated with the kinematic model from [7] (light blue).

The bump stop's jump-in point is indicated by the stiffness rise at approximately 10 mm of wheel-center travel for Var_B and 40 mm for Var_C. As wheel travel increases, the bump stop compresses further, causing the stiffness to progressively increase. The comparison of the curves reveals that, at zero wheel-center displacement (2UP), the wheel rate c_{WC} for Var_C increased by +30.2%, as shown in Table 5. This increase is caused by the parasitic spring rates of the prototype bushings, which are higher than designed, as proven by the light blue and magenta lines in Figure 11a.

The delayed jump-in point for Var_C can be explained by a missing spacer between the bump stop and damper, which was a mistake during installation that was unfortunately identified after all the tests were completed. Furthermore, Var_C shows an increasing wheel rate during rebound, which is a result of the increasing kinematic ratio between the wheel center and the RU bushing.

The evaluation of the suspension roll rate $c_{\phi,WC}$ at the rear, which is defined as the derivative of the rear roll moment with respect to the suspension roll angle (body roll angle without vertical tire effects), is shown in Figure 11b. In this convention, a negative suspension roll angle corresponds to a left turn. The results indicate an increase in the roll rate for $\mathrm{Var_C}$ of about +6.3% at zero suspension roll, which is a result of the increased parasitic spring rate of the prototype bushing differing from the design target value. Additionally, the difference in the bump stop jump-in point between $\mathrm{Var_B}$ and $\mathrm{Var_C}$ is noticeable. For $\mathrm{Var_B}$, $c_{\phi,WC}$ shows a significant increase at a $\approx\pm1°$ roll angle, whereas for $\mathrm{Var_C}$, the jump-in point occurs at a $\approx\pm4°$ roll angle.

Figure 11c,d shows the toe and camber kinematics in comparison between both variants for bounce and roll motion. The results show that the toe gradient $\Delta\delta_{roll}$ and the camber gradient $\Delta\gamma_{roll}$ for roll and bounce motion are very similar for $\mathrm{Var_B}$ and $\mathrm{Var_C}$. The results are shown in Table 5. For comparison, the light blue lines show the kinematic gradients calculated using the method in [7]. The comparison between the kinematic curve and the actual measured curve of the MLTA (red) demonstrates good agreement. Hence, the kinematic calculations from [7] have been validated with the KnC measurements.

Figure 12a illustrates the trajectory of the wheel center during bounce motion in a side view (xy-plane). The results clearly show that, due to the kinematic of the MLTA's longitudinally oriented Watt's linkage (see Figure 3b), $\mathrm{Var_C}$ shows a positive wheel-center recession τ_{wc} compared with the negative recession from $\mathrm{Var_B}$. This fact should have a positive impact on vehicle comfort, especially for single impacts [17]. Again, the kinematic gradient calculated in [7] and highlighted in light blue corresponds well with the measurement result.

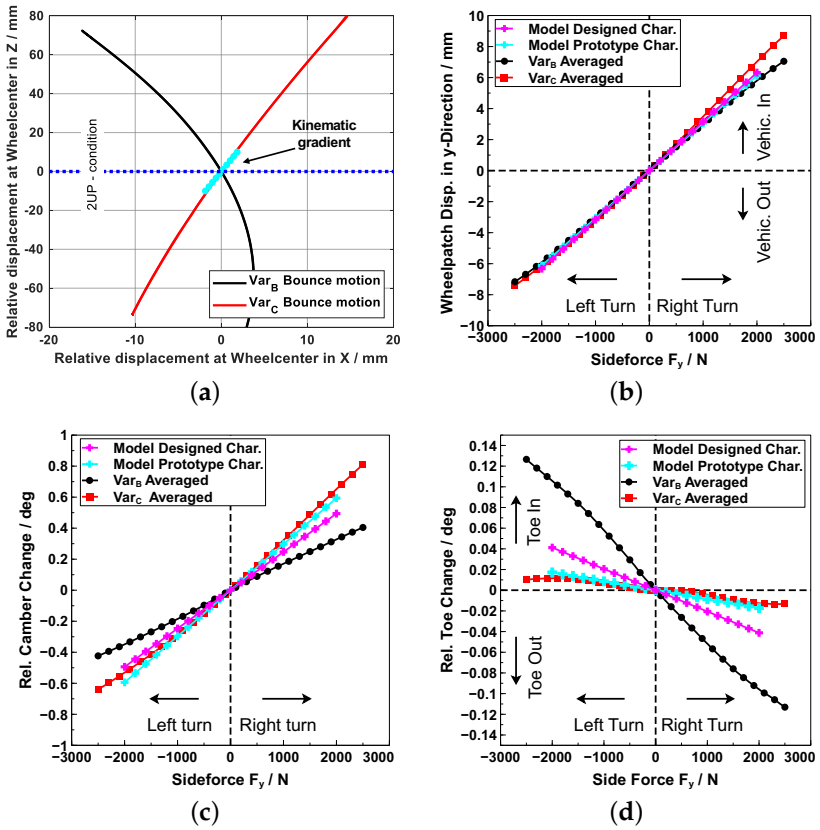


Figure 12. KnC results, comparison between $\mathrm{Var_B}$ and $\mathrm{Var_C}$, and model calculation with designed bushing characteristics (magenta) and with real prototype bushing characteristics (light blue): (**a**) trajectory of the wheel center during bounce motion in xz—side view, (**b**) lateral compliance at the wheel contact patch, (**c**) camber compliance, and (**d**) toe compliance.

Figure 12b shows the lateral displacement at the projected contact patch as a function of lateral force. The results reveal that Variant B (represented in black) and Variant C (depicted in red) are very similar. The magenta line marks the compliance calculated using the modeling approach previously described, incorporating the designed bushing characteristics. The light blue lines represent the compliance achieved with the real prototype bushing characteristics. Notably, both lines align closely with the compliance observed in the measurement results.

Figure 12c,d shows the relative camber and toe change of the left rear wheel as a function of the lateral force at the wheel patch. In addition to the lateral force, an alignment moment was introduced that represents the moment caused by a pneumatic trail of 30 mm.

The camber compliance c_γ shown in Figure 12c increased significantly by +66.7% to 0.3 deg/kN, which should be optimized. The increased compliance can be attributed to the deviation of the RU bushing properties from the design target, which can also be seen from the comparison between the magenta (designed) and light blue (prototype) lines, which reflect the results of the compliance calculation.

The results of the toe compliance measurement showed that the c_δ of $\mathrm{Var_C}$ has decreased significantly compared with $\mathrm{Var_B}$ and is now clearly closer to a neutral toe behavior. This can be explained by the reversed installation direction, which creates a natural toe-in tendency under lateral force for the TBE (see Table 2). The elasto-kinematic bushing setup (especially at U) creates, however, a toe-out tendency. The entire toe compliance of the MLTA is the sum of both effects, detailed in Table 2 and illustrated with the light blue line in Figure 12d. The magenta line corresponds to c_δ using the designed bushing stiffness. This means that a larger toe-in can be achieved when the designed bushing characteristic is met.

The design of the bushings in Section 2.1 was optimized to achieve stiffness characteristics comparable to a TBA. However, because of strong deviations in stiffness characteristics in the real prototype bushings, the design targets could not be fully achieved. Table 5 summarizes the results of the KnC-measurement.

Table 5. Summary of the KnC results in 2UP loading condition.

Characteristic Values	Figure	$\mathrm{Var_B}$	$\mathrm{Var_C}$	C to B
Knc				
c_{WC} Wheel rate (N/mm)	Figure 11a	33.37	43.45	+30.2%
$c_{\phi,WC}$ Roll rate (Nmm/deg)	Figure 11b	1065.14	1132.00	+6.3%
$\Delta\gamma_{roll}$ Camber gradient @ roll (deg/mm)	Figure 11c	-4.71×10^{-2}	-4.93×10^{-2}	−4.7%
$\Delta\delta_{roll}$ Toe gradient @ roll (deg/mm)	Figure 11d	5.20×10^{-3}	5.83×10^{-3}	+12.1%
τ_{wc} Wheel-center recession (mm/m)	Figure 12a	−130	167	+228%
$c_{y,WP}$ Lateral compliance (mm/kN)	Figure 12b	2.94	3.27	+11.2%
c_γ Camber compliance (deg/kN)	Figure 12c	0.18	0.3	+66.7%
c_δ Toe compliance (deg/kN)	Figure 12d	−0.05	−0.01	+80.0%

3.2. Testing at Vehicle Level—Objective Evaluation

3.2.1. Vehicle Instrumentation

Throughout the objective evaluation, a number of different vehicle parameters were measured, depending on the corresponding driving maneuver.

To determine the vehicle fixed velocities in the longitudinal (x) and lateral (y) direction, a correvit sensor was used that was mounted in front of the vehicle (Figure 13a). In combination with the vehicle yaw rate, which was measured with an inertia measurement unit (IMU) (Figure 13b), it was possible to evaluate the vehicle side-slip angle at arbitrary positions on the vehicle body. The steering wheel angle and torque were measured with a steering effort sensor on the steering wheel (Figure 13c). Furthermore, laser distance sensors were installed to measure the vehicle heave motion at the front (dive) and the rear (lift) relative to the ground to determine the total pitch angle of the vehicle (Figure 13d). The lateral acceleration and exact vehicle position were measured with the help of the above-

mentioned inertia measurement unit (IMU) and a dual GPS-antenna setup (Figure 13e). Figure 13f shows the data logger on the passenger seat, which caused an approximately 2UP-loading condition during the objective handling tests.

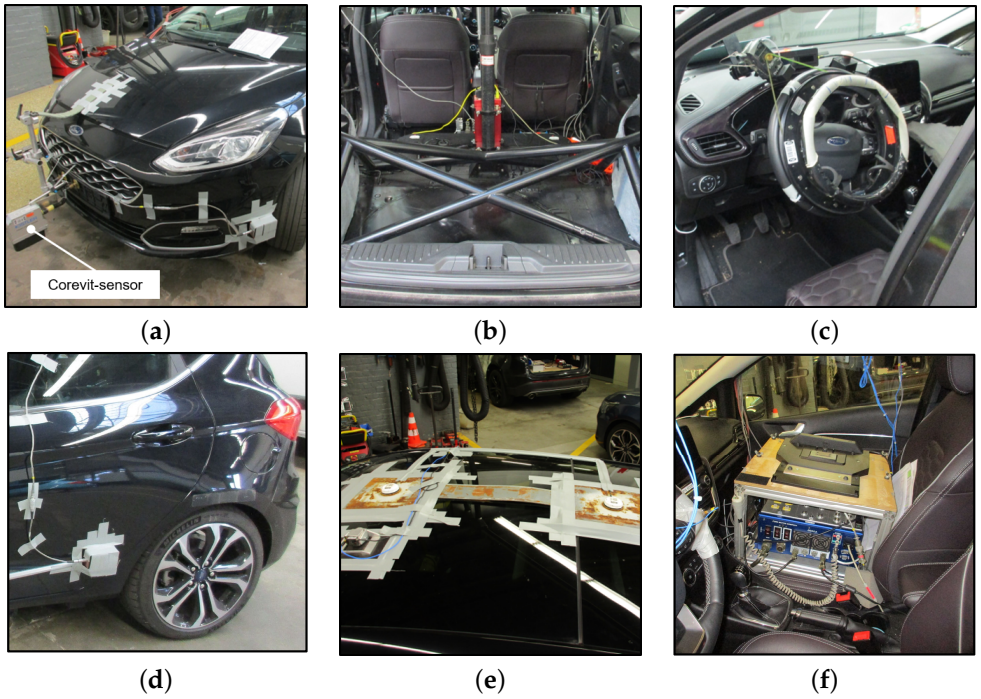


Figure 13. Instrumentation of the prototype vehicle: (**a**) steering effort sensor, (**b**) correvit sensor, (**c**) inertia measurement unit (IMU), (**d**) laser distance sensor at left rear wheel, (**e**) GPS-antenna setup, (**f**) data logger on the passenger seat.

3.2.2. Steady-State Evaluations—Constant-Radius Cornering

The steady-state cornering behavior was evaluated by performing a constant-radius cornering (CRC) maneuver with a radius R of 100 m. Six runs were evaluated in total, with three in each direction (left and right). A polynomial curve was used for regression analysis to fit the test data for both left and right test runs. For clarity, the test results of the left runs were converted into the signs of the right curve by changing the sign convention. A mean curve was then generated based on all six runs and shown in Figure 14, along with the standard deviation $\pm\sigma$ as error bars.

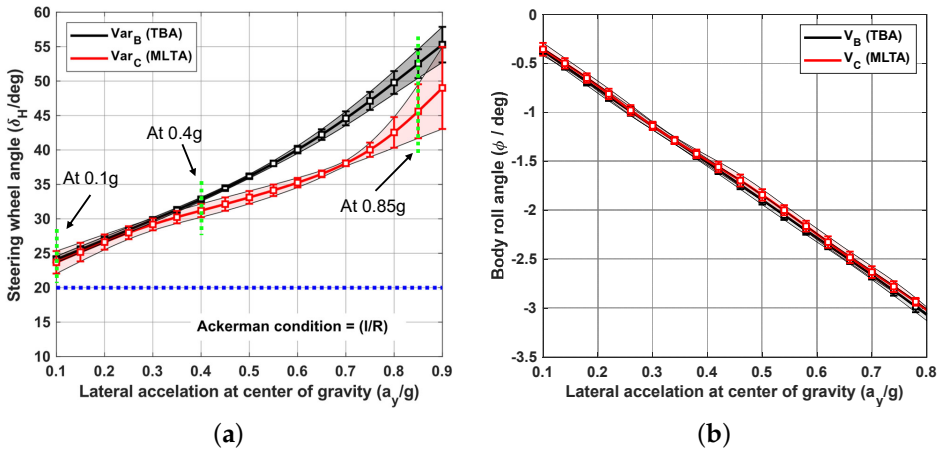


Figure 14. Objective results of the constant-radius cornering maneuver at a 100-m radius: (**a**) steering wheel angle δ_H as a function of the lateral acceleration a_y and (**b**) body roll angle φ as a function of the lateral a_y.

Figure 14a shows the mean curve of steering wheel angle δ_H as a function of the lateral acceleration, a_y, at the center of gravity. Both variants have the same steering ratio, which allows for a direct comparison of the steering wheel angle. The blue line indicates the Ackerman condition, which is defined according to the vehicle length, l, and cornering radius, R. The comparison between both variants clearly shows less understeer tendency in the range from 0.3 to 0.7g for the vehicle equipped with the MLTA ($\mathrm{Var_C}$). This behavior is most likely caused by the different deviations of the MLTA prototype to the optimized design, which leads to an increased slip angle, α_r, at the rear.

However, at higher acceleration levels, the MLTA tends to show a higher understeer tendency. This behavior could be caused by the axial stop of the U bushing (see Figure 6c), resulting in greater axial stiffness.

To quantify the self-steering behavior, the self-steer gradient $\frac{d\delta_H}{da_y}$ was evaluated at three different lateral accelerations, 0.1 g, 0.4 g, and 0.85 g, and listed in Table 6. There, clear differences between $\mathrm{Var_B}$ and $\mathrm{Var_C}$ can be seen. The standard deviation reveals a large degree of scatter in the data for $\mathrm{Var_C}$ above 0.7 g. Therefore, the value at higher accelerations should be interpreted with caution.

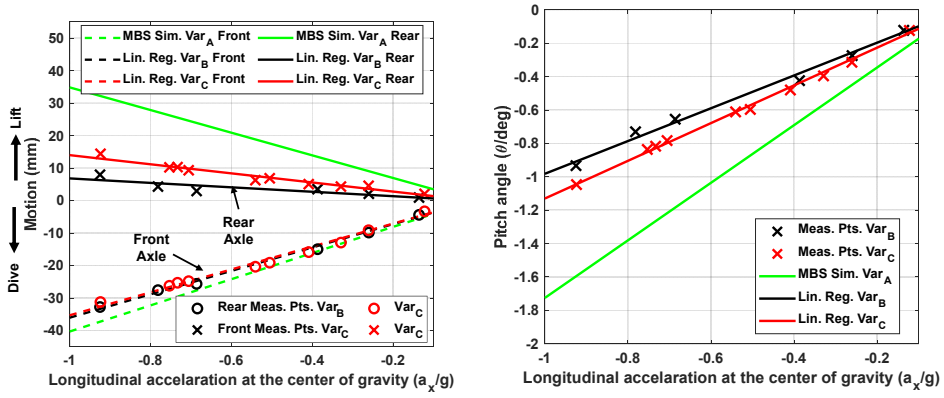
The evaluation of the body roll angle φ in Figure 14b during the constant-radius cornering shows no significant differences between both variants. To quantify this, the roll angle gradient $\Delta\varphi$, which describes the roll angle per lateral acceleration, was evaluated.

The results of all objective driving tests are summarized Table 6.

3.2.3. Steady-State Evaluations—Braking

The kinematic concept of the MLTA, as described in the introduction, aims to maintain the anti-lift behavior of the rear axle at the level of the standard TBA. To validate the kinematic concept and assess the pitch behavior, the vehicle was equipped with laser distance sensors at the front and rear axles to measure the heave motion during braking, as shown in Figure 13d.

The stationary heave motions (after the vehicle stabilized from initial braking overshoot) were measured for $\mathrm{Var_B}$ and $\mathrm{Var_C}$ at various decelerations a_x and shown in Figure 15a. A first-degree polynomial regression was used to fit the measurement points, leading to the dive gradient, $\Delta\kappa_f$, for the front and to the lift gradient, $\Delta\kappa_r$, at the rear axle. Since no measurement results were available for $\mathrm{Var_B}$, the results were obtained using a multibody simulation (MBS).



(**a**) (**b**)

Figure 15. Comparison of straight-line braking results between $\mathrm{Var_A}$ (MBS simulation), $\mathrm{Var_B}$ (Measurement TBA), and $\mathrm{Var_C}$ (Measurement MLTA) linear regression yielded the following: (**a**) front dive $\Delta\kappa_f$ and rear lift $\Delta\kappa_r$ gradients from heave motion and (**b**) pitch gradient $\Delta\theta$ from pitch motion.

The result in Figure 15a clearly shows that both $\mathrm{Var_B}$ and $\mathrm{Var_C}$ show less dive motion at the front and significantly less lift motion at the rear compared to the reference vehicle ($\mathrm{Var_A}$). This reduction in dive and lift motion is attributed to the mass dummy installed,

which lowers the center of gravity (cg_z) by 14% (Table 4), and to the increased spring stiffness compared to Var_A.

The comfort perception during braking is primarily attributed to the vehicle's pitching motion [18], which can be determined straightforwardly from the wheelbase and the heave at the front and rear axles.

The results are illustrated in Figure 15b. The comparison reveals that Var_C exhibits a slightly increased pitching gradient (+10%) compared to Var_B. However, the pitching gradient of both variants, Var_B and Var_C, is significantly below the level of the production vehicle (Var_A).

This confirms the effectiveness of the kinematic concept of the MLTA in achieving good anti-lift behavior. The results of the braking evaluation are summarized in Table 6.

3.2.4. Lateral Transient Response—Frequency Response with Sweep Steer Maneuver

To evaluate the lateral transient driving behavior of the vehicle in the relevant frequency range of 0–3 Hz, a sweep steer test was performed. For this purpose, a steering-wheel angle sweep (0–3 Hz) with an amplitude of ≈16° was applied at a driving speed of 120 km/h (see Figure 16a). Lateral acceleration of ≈0.4 g was achieved in accordance with ISO 7401 [19].

Figure 16a shows the signal for the steering wheel angle and corresponding output signal for a_y in the time domain for one test run. The respective input signal of the steering wheel angle δ_H, which is denoted as $x(t)$, was transformed into the frequency domain $X(f)$ using the fast Fourier transformation (FFT) algorithm. The auto power spectrum $G_{XX}(f)$ can be obtained by multiplying the conjugate complex FFT result $X^*(f)$ with $X(f)$ [20]. Furthermore, the cross-power spectrum, $G_{XY}(f)$, can be calculated from two different signals similarly: multiplying the conjugate complex result, $X^*(f)$, of the FFT with the corresponding output signal, $Y(f)$:

$$G_{XX}(f) = X^*(f) \cdot X(f) \tag{8}$$

$$G_{XY}(f) = X^*(f) \cdot Y(f) \tag{9}$$

Assuming that the output signal shows more dominant noise components compared with the input signal, the complex transfer function, $H(f)$, can be estimated using the following equation:

$$H(f) = \frac{X^*(f) \cdot Y(f)}{X^*(f) \cdot X(f)} = \frac{G_{XY}(f)}{G_{XX}(f)} \tag{10}$$

Figure 16 shows the results of the frequency response test with the test parameters described above. For the evaluation, the gain and phase angle between the input and output signal were determined from the respective transfer function, $H(f)$. The literature suggests evaluating different transfer behaviors for this test, which are expected to show a high correlation to subjective evaluation. Thus, the transfer characteristics between the steering wheel angle δ_H as the input and vehicle lateral acceleration a_y and yaw rate $\dot{\Psi}$ as the output are described as a good correlation to the subjective perceived response of the vehicle [21].

The gain response of a_y is shown in Figure 16b. The frequency spectrum was evaluated from 0.2 to 3 Hz. This particular frequency range was chosen because the steering input signal below 0.2 Hz does not form a significant part of the input signal. The steady-state gain is evaluated using the factor $(\frac{a_y}{\delta_H})_{sts}$ at 0.2 Hz, as indicated with the blue dashed lines. The result shows a slightly higher value for Var_C compared with Var_B by 2.1%. The cutoff frequency $\omega_{ay,c}$, which is defined as the frequency at which the signal power is reduced by −50% (−3 dB), was determined, and no significant difference was found between the two variants.

The phase response of a_y is shown in Figure 16c. Here, the phase shift for Var_C increases at a slower rate compared with Var_B. To quantify this difference, the frequency

$\omega_{eq,ay}$ at which the phase shift reaches −45 was evaluated. The results show that Var_B reaches $\omega_{eq,ay}$ at 0.94 Hz, whereas Var_C reaches the same phase shift at 0.88 Hz.

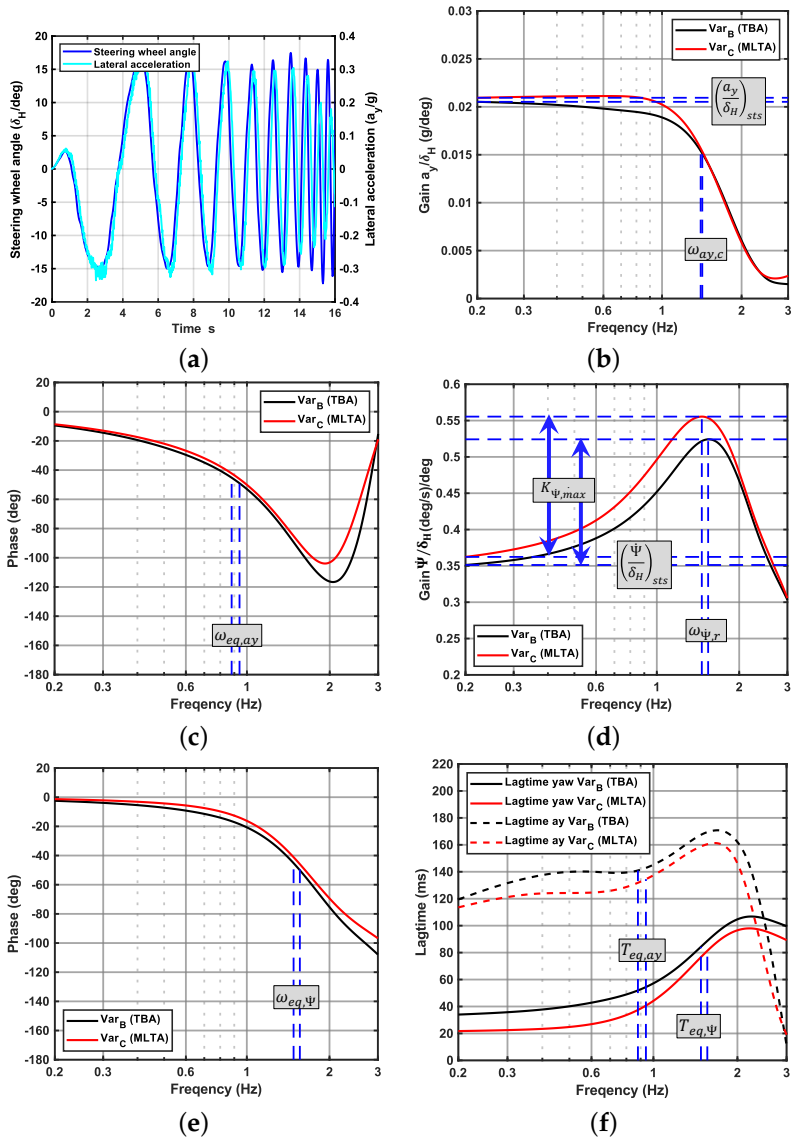


Figure 16. Objective result of the frequency response test at 120 km/h and 0.4 g: (**a**) time signal for the steering wheel angle and the lateral acceleration, (**b**) gain response of lateral acc. a_y, (**c**) phase response of lateral acc. a_y, (**d**) gain response of yaw rate $\dot{\Psi}$, (**e**) phase response of yaw rate $\dot{\Psi}$, and (**f**) lag times for lateral acc. a_y and yaw rate $\dot{\Psi}$.

Figure 16d displays the gain response for the yaw rate. The results reveal a slightly increased steady-state gain factor of $(\frac{\dot{\Psi}}{\delta_H})_{sts}$ (+3.2%) for Var_C compared with Var_B. Additionally, the resonant frequency, $\omega_{\dot{\Psi},r}$, is reduced from 1.54 Hz for Var_B to 1.46 Hz for Var_C. The peak-to-gain ratio, $K_{\dot{\Psi},max}$, also exhibits a slightly increased ratio (+2.7%) for Var_C.

The phase response of the yaw rate is shown in Figure 16e. Similar to the previous results, Var_C shows a slower reduction in the phase shift compared with Var_B. Specifically, the results indicate that Var_C reaches $\omega_{eq,\dot{\Psi}}$ at 1.56 Hz, while Var_B reaches the same phase shift at 1.48 Hz.

To quantify how quickly a system (vehicle) responds to changes in input, one commonly used characteristic is the effective time constant, which is denoted as T_{eq} [22]. This value can be calculated based on the previously evaluated frequencies of $\omega_{eq,\dot{\Psi}}$ and $\omega_{eq,ay}$:

$$T_{eq} = \frac{45^\circ}{360^\circ} \cdot \frac{1}{\omega_{eq}} \tag{11}$$

Figure 16f displays the delay time, which is also known as lag time, along with the corresponding effective time constant marked with a blue dashed line. The results clearly indicate that, over the entire frequency range of 0.2–3 Hz, Var_C exhibits reduced lag times.

Previous studies have evaluated the correlation between subjective ratings and objective results in the frequency response test [22–24]. Based on these results, several recommendations were provided. Specifically, it was advised to avoid a high resonance peak in the yaw gain [25–27], as depicted in Figure 16d. Additionally, the cutoff frequency for lateral acceleration should not be too low [22], as shown in Figure 16b. A small phase shift is generally preferred for achieving an agile driving feel [28].

The evaluation results reveal that Var_C achieves shorter lag times, as presented in Figure 16f. However, the resonance peak for the yaw response is more significant for Var_C compared with Var_B, as depicted in Figure 16d. Moreover, Var_C exhibits higher steady-state gains, leading to the conclusion that MLTA provides a more agile driving feel than Var_B. All findings are summarized in Table 6.

Table 6. Summary of the objective driving evaluation.

Characteristic Values	Figure	Var_A	Var_B	Var_C	C to B
Constant-radius cornering (CRC)					
$(\frac{d\delta_H}{da_y})_{0.1}$ Self-steering gradient @ 0.1g (deg/g)	Figure 14a		29.0	30.0	+3.4%
$(\frac{d\delta_H}{da_y})_{0.4}$ Self-steering gradient @ 0.4g (deg/g)	Figure 14a		31.0	19.0	−38.7%
$(\frac{d\delta_H}{da_y})_{0.85}$ Self-steering gradient @ 0.85g (deg/g)	Figure 14a		55.0	66.0	+20.0%
$(\Delta\varphi)$ Roll gradient (deg/g)	Figure 14b		−3.85	−3.81	−1.0%
Straight-line braking (SLB)					
$\Delta\kappa_f$ Dive gradient (mm/g)	Figure 15a	40.3	36.0	35.3	−1.9%
$\Delta\kappa_r$ Lift gradient (mm/g)	Figure 15a	−34.9	−6.8	−14.0	−105.9%
Hip-point rise gradient (mm/g)	Figure 15a	−0.1	15.40	11.6	−24.7%
$\Delta\theta$ Total pitch gradient (deg/g)	Figure 15b	1.7	1.0	1.1	10%
Frequency response (FR)					
$\omega_{ay,c}$ Cut-off frequency (Hz)	Figure 16b		1.42	1.4	−1.4%
$\omega_{\Psi,r}$ Resonant frequency (Hz)	Figure 16d		1.54	1.46	−5.2%
$(\frac{a_y}{\delta_H})_{sts}$ Gain for lateral acc. (g/deg)	Figure 16b		2.05×10^{-2}	2.09×10^{-2}	2.1%
$(\frac{\Psi}{\delta_H})_{sts}$ Gain for yaw rate (deg/s)/deg	Figure 16d		3.51×10^{-1}	3.62×10^{-1}	3.2%
$K_{\Psi,max}$ Gain ratio (−)	Figure 16d		1.49	1.53	2.7%
$T_{eq,ay}$ Effective time constant (ms)	Figure 16f		141	135	−4.6%
$T_{eq,\Psi}$ Effective time constant (ms)	Figure 16f		84	81	−3.6%

4. Subjective Evaluation of the MLTA Prototype

In addition to the objective driving tests, subjective driving tests were also carried out. At the beginning of the development, trained expert drivers drove the mass dummy modified vehicle (Var_B) and compared it with the standard reference vehicle (Var_A) to quantify the influence of the additional masses on the subjective evaluation. After that, the mass-modified vehicle was equipped with the MLTA (Var_C) and evaluated in the same way. The results are shown in Figure 17 as relative values due to the confidentiality of the absolute data. Var_A (green curve) serves as the baseline, while the rating for Var_B is shown in black and the rating for Var_C in red. All reference values for Var_A were set to 5, and the deviations for Var_B and Var_C are depicted relative to these baseline values. The ratings can, thus, be directly compared. The differences in ratings between the variants are shown on the right side of the snake chart.

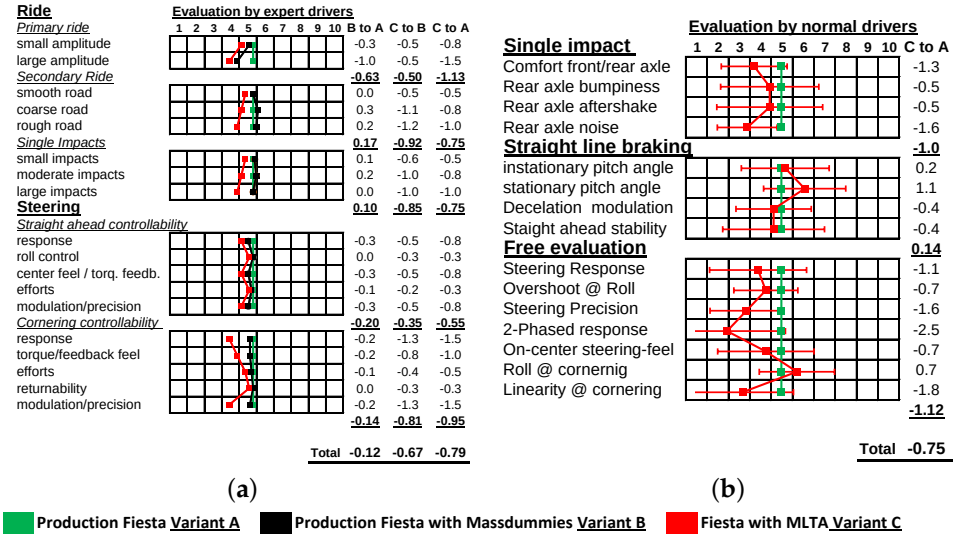


Figure 17. Subjective evaluation results shown in relative values; Var_A (green curve) serves as a reference with all values set to 5: (**a**) ride and steering evaluation by expert drivers; (**b**) evaluation by normal drivers regarding single impacts, straight-line braking, and free evaluation.

4.1. Var_A to Var_B Evaluation—Experts

The results in Figure 17a show that Var_B's increased mass (see Table 4 for variant configuration) negatively impacted the ride evaluation compared with Var_A. The primary ride received a lower rating because the spring and damper of Var_B were not fine-tuned to the increased weight of the vehicle or the new mass distribution and inertia, as shown in Table 4. However, single impacts and secondary ride behavior were rated slightly better than the production vehicle due to the increased mass.

The steering evaluation for Var_B shows slightly worse behavior in straight-line and cornering controllability. The time delay in the response from the rear axle to the front axle was especially noted. This was mainly caused by the increased mass inertia and the damper setup, which was not adjusted accordingly. In total, the mass-added Var_B achieved 0.12 grade less in performance than the series Var_A.

4.2. Var_A to Var_C Evaluation—Experts

At the end of the development, the MLTA-equipped vehicle Var_C was also evaluated by expert drivers and compared with vehicle Var_A. Across all categories, the MLTA was rated worse. In particular, for ride performance, the bump stop characteristic was noted negatively because it responded too progressively. This subjective feeling can be explained by the KnC results concerning the wheel rate in Figure 11a: The bump stop rate and the RU bushing's torsional rate increased with increasing bounce and rebound. This led to an increase in the parasitic spring rate and, thus, a negative impact on ride comfort.

Concerning the steering evaluation, Var_C performed worse straight ahead, especially in cornering controllability. The drivers criticized the vehicle's strong progressive response behavior in cornering, which is reflected in a significantly lower rating, as depicted in Figure 17a. This feeling can be explained by the results of the frequency response test, which revealed increased steady-state gains for the lateral acceleration $(\frac{a_y}{\delta_H})_{sts}$ shown in Figure 16b and the yaw gain $(\frac{\dot{\Psi}}{\delta_H})_{sts}$ shown in Figure 16d. This was most likely caused by tolerances of different components of the MLTA prototype in terms of precision and stiffness (see the end of Section 2.2.2).

Moreover, the drivers criticized the unbalanced setup from the front to the rear axle, which was particularly noticeable during the straight-ahead evaluation. This issue was most likely caused by the prototype vehicle's non-series-tuned spring, damper, and stabilizer setup. In addition, the modulation and precision of Var_C were rated worse, which was

likely caused by the increased camber compliance, as shown in the results of the kinematic and compliance (KnC) tests (see Figure 12c and Table 5).

In total, the MLTA Var_C was rated 0.79 grade lower than the series Var_A and 0.67 lower than Var_B. However, according to the expert drivers, the deficits described above were acceptable for a single-piece prototype without any tuning of components because the performance deviations were mostly in a "tuneable" range.

4.3. Var_A to Var_C Evaluation—Normal Drivers

In addition to the expert driver's evaluations, the MLTA-equipped prototype vehicle was evaluated by 11 "normal" drivers compared with a production vehicle. The evaluation sheet was modified because of the changed track conditions (Figure 17b). It is worth noting that a wide scattering of the results is typical for evaluations by normal drivers [21]. In total, three maneuvers were driven, whereas different characteristics had to be evaluated for the single maneuvers.

During the first test, which involved a single impact at 30 km/h, the results were largely in agreement with those obtained by expert drivers. On average, the MLTA (Var_C) was rated −1 grade worse compared with the −0.75 rating from the expert drivers (see Figure 17a). During the second test, the drivers were asked to rate the pitch and braking behavior of the vehicles. The drivers noticed a smaller stationary pitch angle of Var_C and rated it +1.1 better than Var_A. This observation is supported by the evaluation of the objective data (see Figure 15 and Table 6). During the free evaluation, the drivers evaluated the driving behavior of the vehicles on a forest track based on seven different criteria. The impact of the additional masses was evident, with the lower center of gravity reducing the vehicle's tendency to roll.

Overall, the normal drivers rated Var_C −0.75 grade lower than the production vehicle Var_A, while the expert drivers had very similar results, with Var_C rated −0.79 grade lower than Var_A and −0.67 lower than Var_B.

5. Summary and Conclusions

Based on a novel concept of MLTA for rear suspension for the application in BEVs, and the previously developed calculation approach for the kinematic of the axle, in this work, an elastokinematic calculation concept has been introduced. With this concept, the targeted stiffness characteristics of rubber bushings were calculated, and the corresponding design was proposed. All components of the MLTA were made using a prototyping method and manually welded and assembled. One single prototype vehicle based on Ford Fiesta 2020 with MLTA and modified BIW was built. Due to the manual method and prototyping process, deviations concerning dimensional tolerances and stiffness characteristics from the targeted values that were calculated with the elastokinematic and MBS methods occured.

The vehicle dynamic performance of this prototype vehicle with MLTA (Var_C) was evaluated both objectively and subjectively, and it was compared with a series-production Ford Fiesta (Var_A) and with added mass simulating the mass and mass distribution of a BEV (Var_B).

The objective evaluation through KnC tests shows the following:

- The wheel rate c_{WC} was 30% higher and the camber compliance c_γ was 60% higher than Var_B. Both deviations can be attributed to the tolerances in MLTA, especially the reduced stiffness of the elastomer bushings compared to the target stiffness values.
- Together with the missing bump stop spacer for Var_C, its wheel rate–wheel center displacement curves are different, as well as the roll rate–roll angle characteristics.
- The kinematic toe and camber gradients of MLTA are similar to Var_B.
- The wheel center recession characteristic was considerably improved, thus confirming the MLTA concept.

The objective driving tests of Var_B and Var_C show the following results:

- The constant-radius cornering tests show a reduced understeer of Var_C compared with Var_C that can be explained by the KnC findings.
- In a straight-line braking maneuver, the MLTA (Var_C) shows a 35% lower pitch gradient than Var_A and a 10% higher gradient than Var_B.
- The results of the frequency response test based on a sweep steer input indicate an increased yaw gain and resonance peak. However, the lateral acceleration and yaw rate response times were reduced overall, leading to the conclusion that the MLTA vehicle should be more agile than Var_B.

Finally, expert and normal drivers evaluated the test vehicle subjectively, comparing Var_B and Var_C to the series-production vehicle Var_A. Overall, the MLTA vehicle was rated -0.79 (by experts) and -0.75 (by normal drivers) lower than the series-production vehicle (Var_A). These differences were caused by the deviation between prototype characteristics (stiffness, dimensional tolerances, etc.) and the optimized and targeted design. The study's prototype axle was the first and only prototype axle to be manufactured without any tuning. With the elimination of the defects and additional follow-up tuning of the spring and damper setup, which is a typical part of series vehicle development, the MLTA should be able to reach production-level performance.

Author Contributions: Conceptualization, J.O. and X.F.; methodology, J.O.; software, J.O.; validation, J.O.; formal analysis, J.O.; investigation, J.O.; resources, X.F.; data curation, J.O.; writing—original draft preparation, J.O.; writing—review and editing, X.F.; visualization, J.O.; supervision, X.F.; project administration, X.F.; funding acquisition, X.F. All authors have read and agreed to the published version of the manuscript.

Funding: This work was supported by the European Regional Development Fund under Grant EFRE-0801202.

Data Availability Statement: The datasets presented in this article are not readily available because they contain confidential information that is subject to privacy or proprietary restrictions.

Acknowledgments: This work was made possible through the financial support of the European Regional Development Fund (EFRE, E-MLTA No. EFRE-0801202). We extend our gratitude to our industrial partners, including Ford, Vorwerk Autotec, CP Tech, Mubea, and Schmedthenke Werkzeugbau, for conducting all hardware work. We also express our appreciation to the team at the Ford Lommel proving ground for their invaluable assistance in conducting the objective and subjective driving tests with expert drivers. Additionally, we would like to thank J. Betzler from TH-Köln, T. Küppers and I. Papić from Ford, and T. Kersten and U. Huebner from Volkswagen for their insightful discussions and contributions. Our special thanks also go to G. Coellen and S. Ort from Vorwerk Autotec for their great support and for supplying the prototype bushings, and Mr. Blomenkamp of CP-Tech for the prototyping of the MLTA. Finally, we would like to acknowledge T. Niessing for his valuable contributions and engaging discussions.

Conflicts of Interest: The authors declare no conflicts of interest.

Glossary

The following abbreviations are used in this manuscript:

TBA	Twist-beam axle
BEV	Battery electric vehicle
KnC	Kinematic and compliance
MBS	Multibody simulation
MEB	Modular electric drive matrix
CLA	Composite leaf spring axle
MLTA	Multi-link torsion axle
MLA	Multi-link axle
OEM	Original equipment manufacturer
WCA	Wheel carrier
WP	Wheel patch

EEM	Elastic equivalent mechanism
DOF	Degree of freedom
PWT	Parallel wheel travel
OWT	Opposite wheel travel
WC	Wheel center
BC	Boundary condition
TBE	Twist-beam equivalent
LL	Longitudinal link
SC	Shear center
WN	Wheel normal
BIW	Body in white
U	Upper body mount
L	Lower body mount
RU	Upper wheel carrier point middle
RUi	Upper wheel carrier point inner
RUo	Upper wheel carrier point outer
RL	Lower wheel carrier point
G	Global coordinate system
IC	Instantaneous center of motion
$\mathrm{Var_A}$	Variant A
$\mathrm{Var_B}$	Variant B
$\mathrm{Var_C}$	Variant C
ICE	Internal combustion engine
IMU	Inertia measurement unit
CRC	Constant-radius cornering
FFT	Fast Fourier transformation
PSD	Power spectral density

The following symbols are used in this manuscript:

Notation	**Description**	**Unit**
F_x	Braking force at the wheel patch	N
ΔF_z	Wheel load change caused by load transfer	N
$\underline{F}_{res}$	Resulting force vector at the wheel patch during braking	N
$\underline{F}_{susp}$	Force that is counteracted via the suspension	N
$F_{z,SP,WP}$	Force vertical direction at the wheel patch that needs to be counteracted via the spring	N
$\underline{F}_{SP,WCA}$	Spring force at the wheel carrier (spring attachment)	N
i_{SP}	Kinematic spring ratio between spring position and the wheel patch	–
ε_i	Ideal brake support angle	deg
ε_{Br}	Brake support angle resulting from the suspension geometry	deg
$\underline{e}_{SP}$	Unit vector oriented in the spring direction	mm
κ_r	Anti-lift ratio at the rear axle	%
$\Delta\kappa_f$	Dive gradient at the front axle	deg/mm
$\Delta\kappa_r$	Lift gradient at the rear axle	deg/mm
θ	Pitch angle of the vehicle	deg
$\Delta\theta$	Pitch angle gradient	deg/g
φ	Body roll angle of the vehicle	deg
$\Delta\varphi$	Roll angle gradient	deg/g
Ω_{pwt}	DOF rotation axis for parallel wheel travel	–
Ω_{owt}	DOF rotation axis for opposite wheel travel	–
ε_z	First Euler rotation angle around the z-axis (Z-X′-Z″) convention	deg
$\varepsilon_{x'}$	Second Euler rotation angle around the x'-axis (Z-X′-Z″) convention	deg
$\varepsilon_{z''}$	Third Euler rotation angle around the z''-axis (Z-X′-Z″) convention	deg
m_{BP}	Mass of the battery pack	kg
m_{ICE}	Mass of the internal combustion engine	kg
m_{FT}	Mass of the fuel tank	kg
m_{MD}	Overall mass of the mass dummies	kg

m_V	Overall mass of the vehicle	kg
m_f	Front axle load	kg
m_r	Rear axle load	kg
cg	Center of gravity	mm
$\mathbf{I}$	Inertia tensor	kg·mm^2
$\mathbf{C}_{TBE}$	12x12 Compliance matrix to represent the TBE structure	
$\mathbf{A}_R$	Coefficient matrix for reaction force calculation	
$\mathbf{A}_q$	Coefficient matrix for deformation velocity calculation	
$\underline{b}_R$	Constant vector for reaction force calculation	
$\underline{b}_q$	Constant vector for deformation velocity calculation	
$\underline{F}_R$	Global reaction force and moment vector	
$\underline{F}_e$	Input force corresponding to the different load cases	
$\underline{\dot{q}}$	Velocity vector for the multibody system caused by elastic deformation velocity	
c_{WC}	Wheel rate: force gradient in vertical direction at the wheel center during bounce motion	N/mm
$c_{\phi,WC}$	Roll rate: moment gradient in vertical direction at the wheel center during roll motion	N·mm/deg
c_γ	Camber compliance	deg/kN
c_δ	Toe compliance	deg/kN
$c_{y,WP}$	Lateral compliance at the wheel patch position	mm/kN
$\Delta\gamma_{roll}$	Camber gradient: camber angle change during roll motion	deg/mm
$\Delta\delta_{roll}$	Toe gradient: toe angle change during roll motion	deg/mm
δ_0	Static toe angle	deg
γ_0	Static camber angle	deg
τ_{wc}	Wheel center recession: ratio longitudinal to vertical wheel center motion	mm/m
δ_H	Steering wheel angle	deg
a_x	Longitudinal acceleration at the center of gravity	g
a_y	Lateral acceleration at the center of gravity	g
$\frac{d\delta_H}{da_y}$	Self-steering gradient	deg/g
β_h	Side slip angle at the driver's hip point	deg
$\frac{d\beta_h}{d\delta_H}$	Side slip angle gradient at the driver's hip point	deg/deg
R	Cornering radius	m
l	Vehicle length: front wheel center to rear wheel center	m
α_r	Vehicle side slip angle at the rear	deg
α_f	Vehicle side slip angle at the front	deg
l_{cvs}	Distance from the correvit sensor to the front wheel center	m
$\underline{v}_{cvs}$	Velocity vector measured from the correvit sensor	m/s
$\dot{\Psi}$	Yaw rate measured from the IMU	deg/s
$c_{\alpha,f}$	Cornering stiffness at the front	N/deg
$c_{\alpha,r}$	Cornering stiffness at the rear	N/deg
$\omega_{ay,c}$	Cut-off frequency: reduction in the signal power, -3dB	Hz
$\omega_{\dot{\Psi},r}$	Resonant frequency of the yaw rate	Hz
$(\frac{\dot{\Psi}}{\delta_H})_{sts}$	Steady-state gain of the yaw rate	(deg/s)/deg
$(\frac{a_y}{\delta_H})_{sts}$	Steady-state gain of the lateral acceleration	g/deg
$K_{\dot{\Psi},max}$	Peak-to-gain ratio	
T_{eq}	Effective time constant: lag time at 45° phase angle	ms
$x(t)$	Signal x in the time domain	
$X(f)$	Signal x in the frequency domain	
$X^*(f)$	Conjugate complex signal x in the frequency domain	
$G_{XX}(f)$	Auto-power spectrum	
$G_{XY}(f)$	Cross-power spectrum	
Δf	Bandwidth of the frequency bin (frequency resolution of the FFT)	Hz
Fs	Sample rate of the time signal	Hz
N	Number of discrete FFT points	
$H(f)$	Complex transfer function	

References

1. European Commission. *Fit for 55: Delivering the EU's 2030 Climate Target on the Way to Climate Neutrality*; European Commission: Brussels, Belgium, 2021.
2. Kraftfahrt-Bundesamt. *Fahrzeugzulassungen Im Dezember 2021—Jahresbilanz: Press Release Nr. 1/2022*; Technical Report; Kraftfahrt-Bundesamt: Flensburg, Germany, 2022.
3. Wilmes, M.; Kraaijeveld, R.; Schrage, M.; Schummers, F. Challenges and Solutions of Converting Conventional Vehicles to Hybrid Electric or Battery Electric Vehicles. In Proceedings of the 10th International Munich Chassis Symposium, Munich, Germany, 25–26 June 2019; Pfeffer, P.E., Ed.; Springer Fachmedien Wiesbaden: Wiesbaden, Germany, 2020; pp. 343–353. [CrossRef]
4. Hacker, C.; Hofmann, P.; Krahn, S.; Lobo Casanova, I. Composite Leaf Spring Axle für Pkw: Glasfaserverstärkt. *Lightweight Des.* **2015**, *8*, 14–19. [CrossRef]
5. Ditzer, B.; Rosta, S.; Koopmann, J. Leichtbau von Tragfedern für Plug-in-Hybrid- und Elektrofahrzeuge. *Automobiltechnische Zeitschrift* **2022**, *124*, 50–55. [CrossRef]
6. Fang, X.F. Rear Suspension for Electric Vehicle and Vehicle Body. Patent CN105365543A, 2 March 2016.
7. Niessing, T.; Fang, X.F. Kinematic Analysis and Optimisation of a Novel Multi-Link Torsion Axle. *Mech. Mach. Theory* **2021**, *165*, 104432. [CrossRef]
8. Olschewski, J.; Fang, X.F. Elastokinematic design and optimization of the multi-link torsion axle—A novel rear axle concept for BEVs. *Mech. Based Des. Struct. Mach.* **2024**, 1–32. [CrossRef]
9. Fang, X.F.; Tan, K. Analytical Modelling of Twist Beam Axles. *Int. J. Veh. Syst. Model. Test.* **2018**, *13*, 1–25. [CrossRef]
10. Seth, M.K.; Glorer, J.; Schellhaas, R. Design of A New Weight and Cost Efficient Torsion Profile for Twistbeam Suspension. In Proceedings of the WCX™17: SAE World Congress Experience, Detroit, MI, USA, 4–6 April 2017. [CrossRef]
11. A2Mac1. 3D-Scan, Opel Ampera-e, 2018.
12. Lu, Y.; Rong, X.; Hu, Y.S.; Chen, L.; Li, H. Research and Development of Advanced Battery Materials in China. *Energy Storage Mater.* **2019**, *23*, 144–153. [CrossRef]
13. International Energy Agency. *Global EV Outlook 2023: Catching Up with Climate Ambitions*; Global EV Outlook; International Energy Agency: Paris, France, 2023. [CrossRef]
14. Wang, C.; He, L.; Sun, H.; Zhu, J.; Lu, Z.; Zhu, Y.; Hu, S. A kind of Lithium Ion Battery, Battery Module, Battery Pack and Automobile. Chinese Patent CN110518156A, 29 November 2019.
15. Sumpf; Pires, A.; Stockton, W.B.; Spooner, C.; Prodan, C.; Gorasia, J.B.; Harris, K.; Burke, D.; Szafer, D.G.; Patel, K.; et al. Integrated Energy Storage System. U.S. Patent WO2021102340A1, 27 May 2021.
16. Wassiliadis, N.; Steinsträter, M.; Schreiber, M.; Rosner, P.; Nicoletti, L.; Schmid, F.; Ank, M.; Teichert, O.; Wildfeuer, L.; Schneider, J.; et al. Quantifying the State of the Art of Electric Powertrains in Battery Electric Vehicles: Range, Efficiency, and Lifetime from Component to System Level of the Volkswagen ID.3. *eTransportation* **2022**, *12*, 100167. [CrossRef]
17. Matschinsky, W. *Radführungen Der Straßenfahrzeuge*, 3rd ed.; Springer: Berlin/Heidelberg, Germany, 2007.
18. Tavernini, D.; Velenis, E.; Longo, S. Feedback Brake Distribution Control for Minimum Pitch. *Veh. Syst. Dyn.* **2017**, *55*, 902–923. [CrossRef]
19. *DIN ISO 7401*; Straßenfahrzeuge: Testverfahren Für Querdynamisches Übertragungsverhalten. ISO: Geneva, Switzweland, 1989.
20. Havelock, D.; Kuwano, S.; Vorländer, M. (Eds.) *Handbook of Signal Processing in Acoustics*, 1st ed.; Springer: New York, NY, USA, 2016.
21. Decker, M. Zur Beurteilung Der Querdynamik von Personenkraftwagen. Ph.D. Thesis, Technische Universität München, Munich, Germany, 2009.
22. Weir, D.H.; Dimarco, R.J. Correlation and Evaluation of Driver/Vehicle Directional Handling Data. In Proceedings of the 1978 Automotive Engineering Congress and Exposition, Detroit, MI, USA, 1 February 1978; p. 780010. [CrossRef]
23. Chen, D.C.; Crolla, D.A. Subjective and Objective Measures of Vehicle Handling: Drivers & Experiments. *Veh. Syst. Dyn.* **1998**, *29*, 576–597. [CrossRef]
24. Becker, K. (Ed.) *Subjektive Fahreindrücke Sichtbar Machen IV: Korrelation Zwischen Objektiver Messung und Subjektiver Beurteilung in der Fahrzeugentwicklung*; Number 4 in Subjektive Fahreindrücke Sichtbar Machen; Expert: Renningen, Germany, 2010.
25. Schindler, E. *Fahrdynamik: Grundlagen Des Lenkverhaltens Und Ihre Anwendung Für Fahrzeugregelsysteme*, 3rd ed.; Expert: Tübingen, Germany, 2019.
26. Mimuro, T.; Ohsaki, M.; Yasunaga, H.; Satoh, K. Four Parameter Evaluation Method of Lateral Transient Response. In Proceedings of the Passenger Car Conference & Exposition, Dearborn, MI, USA, 17–20 September 1990; p. 901734. [CrossRef]
27. Barter, N.F. Analysis and Interpretation of Steady-State and Transient Vehicle Response Measurements. *Veh. Syst. Dyn.* **1976**, *5*, 79–103. [CrossRef]
28. Mitschke, M.; Wallentowitz, H. *Dynamik Der Kraftfahrzeuge*, 5th ed.; Springer Vieweg: Wiesbaden, Germany, 2014.

Disclaimer/Publisher's Note: The statements, opinions and data contained in all publications are solely those of the individual author(s) and contributor(s) and not of MDPI and/or the editor(s). MDPI and/or the editor(s) disclaim responsibility for any injury to people or property resulting from any ideas, methods, instructions or products referred to in the content.